Electric field effect on the microstructure and properties of $Ba_{0.9}Ca_{0.1}Ti_{0.9}Zr_{0.1}O_3$ (BCTZ) lead-free ceramics.

A. Reyes-Montero[1], F. Rubio-Marcos[2], L. Pardo[3], A Del Campo[2], R. López-Juárez[4] and M.E. Villafuerte-Castrejón[1].

[1]Instituto de Investigaciones en Materiales, Universidad Nacional Autónoma de México, Circuito Exterior S/N, A.P. 70-360, CDMX, México.
[2]Electroceramic Department, Instituto de Cerámica y Vidrio, CSIC, 28049 Madrid, España.
[3]Instituto de Ciencia de Materiales de Madrid, CSIC, c/ Sor Juana Inés de la Cruz, 3, Cantoblanco, 28049 Madrid, España.
[4]Unidad Morelia del Instituto de Investigaciones en Materiales, Universidad Nacional Autónoma de México, Antigua Carretera a Pátzcuaro No. 8701, Col. Ex Hacienda de San José de la Huerta, C.P. 58190 Morelia, México.

ABSTRACT: The attention in piezoelectric devices has been moved in the past decade to lead-free ceramics, especially on (Ba,Ca)(Ti,Zr)O_3-based materials, due to growing environmental concerns. Here we report a systematic evaluation of the effect that the electric field application has on the structure, microstructure and electrical properties in $Ba_{0.9}Ca_{0.1}Ti_{0.9}Zr_{0.1}O_3$ (BCTZ) lead–free ceramics. Powders were prepared by Pechini method. Dense ceramic samples were sintered at 1275°C for 5h. As observed by X-ray diffraction (XRD) and energy dispersive x-ray spectroscopy (EDS), the ceramics are single perovskite-type structure phase and they are homogeneous both at global and local scale. Rietveld analysis of the diffraction patterns for the non-poled sample is consistent with a coexistence of ferroelectric tetragonal *P4mm* and rhombohedral *R3m* symmetries. It is shown that electric field induces changes in rhombohedral–tetragonal relative content that facilitates polarization process of the system. Ceramics exhibit a significant high piezoelectric response with a d_{33} value as high as ~390pC/N, which is comparable to soft $Pb(Zr_{1-x}Ti_x)O_3$ (PZTs). Scanning Electron Microscopy (SEM) analysis showed an average grain size of 20 μm and complex ferroelectric domains. A confocal Raman spectroscopy and imaging study carried out on both types of samples reveals that, upon application of an electric field, the $E(LO_3)$ +$A_1(LO_2)$ +$E(TO_4)$ mode of the Raman spectra shifts to lower frequencies, indicating a reduction of the bonding force between the ions at the B-site of the perovskite (Ti^{4+}, Zr^{4+}) and the oxygen ions of the octahedron for the poled samples. Besides, the spatially resolved mentioned mode of the Raman spectra shows a narrower distribution in the poled sample, monitoring the polarization alignment effect in the direction of the field. These characteristics are related with the complex ferroelectric domain distribution. The polar structure changes after the application of the electric field is revealed, as well by the changes on the dielectric permittivity curves as a function of the temperature. Ceramics also displays a high ferroelectric remnant polarization (P_r=15.3 μC/cm^2) and low coercive field (E_C=1.5 kV/cm) at room temperature.

KEYWORDS: Ferroelectrics, Piezoelectrics, Dielectrics, Lead-Free, BCZT, Phase Transitions, X-ray Diffraction, Raman Spectroscopy.

INTRODUCTION

Lead-based piezo-ferroelectric materials are widely common employed for many high performance applications[1] including nanotechnology[2], which has opened to new advanced functions based upon existing piezoelectric skills. However, many regulations have been made to forbid lead-based materials because of their toxicity[1]. **Environmental and especially the human health concerns are the imperative driving force for eliminating lead from current commercial piezoelectric materials. Since then, lead-free materials have attracted much attention and many researchers have attempted to introduce them in suitable sustainable devices[3-7].**

It should be highlighted that piezoceramic systems are technologically interesting. Many actuator applications require high electromechanical coupling factor (e.g. fuel injection, ultrasonic motor, etc.). This is largely fulfilled by piezoelectric materials, which allow direct conversion between electrical and mechanical energy. Moreover, modern technologies have evolved towards energy harvesting using different piezo-ferroelectric elements. This characteristic has gained great interest in recent years by offering a way of supplying sensor systems without the need of batteries and maintenance[8]. The energy obtained from diverse sources including human activity, industrial machinery movement and environmental vibrations[9,10] could be harvested and stored through micro generators[11]. For this reason, the development of many piezo-ferroelectric lead-free materials, as $(Ba,Ca)(Ti,Zr)O_3$ with large d_{33} and g_{33} (which contribute to the figure of merit for energy harvesting) should address more optimum operation conditions, basically higher amplitudes and frequencies of the driving electric field as well as a large mechanical stress[12].

In the past decade, with the objective of achieving a significant improvement in the piezoelectric activity of $BaTiO_3$-based ceramics, much attention has been given to the construction of phase boundaries driven by composition modifications[13]. Among them, noticeably, the $(Ba_{1-x}Ca_x)(Ti_{1-y}Zr_{y)}O_3$ system has open a path for many research activities because of the large piezoelectric response produced by some compositions proximity to a triple point (TP), characterized by rhombohedral (R), tetragonal (T) and cubic phases coexistence[14]. This system has achieved great attention due to the possibility of tailoring the piezo-ferroelectrical properties by controlling the system stoichiometry[15].

$(Ba_{1-x}Ca_x)(Ti_{1-y}Zr_{y)}O_3$ ceramics have been of interest after a high piezoelectric coefficient (d_{33}~620 pC/N) was reported for the Morphotropic Phase Boundary (MPB) composition[14]. The flattening of the free-energy levels profiles between two ferroelectric phases (produced at the MPB)[16] and a field-induced structural transformation (by the polarization/rotation effect)[17] are the main responsible factors of the strong electromechanical activity in PZT systems. However, the extrinsic contribution, especially the one associated with the reversible domain wall motion, plays a dominant role for the high piezoelectric response in $(Ba_{1-x}Ca_x)(Ti_{1-y}Zr_{y)}O_3$ ceramics[18].

Electric field effects on the global crystal structure **in the MPB composition** ($Ba_{0.85}Ca_{0.15}Ti_{0.90}Zr_{0.10}O_3$) has been previously observed by means of X-ray diffraction[19] and Raman spectroscopy[20]. These techniques have been used to clarify the controversy on the phase transitions and the origin of high piezoelectricity at the MPB on different lead-based materials. The electric field makes the ferroelectric-ferroelastic domain walls move, developing a preferred orientation on the poled ceramics manifested in the diffraction pattern as alternation in the ratio of the intensities of the Bragg profiles[17,21]. **Besides, some lead-free materials, which in the unpoled state present a coexistence of crystal symmetries, undergoes a field-induced phase transition to the most ferroelectrically distorted one, at the expenses of the weakly polar ones, that can be analyzed by X-ray diffraction[22-24]. Such a field-induced phase transition provides an additional contribution to the piezoelectric effects presented by these lead-free ceramics.** Alternatively, the Raman detects variations of the Ti^{4+}-O^{2-} longitudinal optical (LO) mode related to ferroelectric phase transformations[25]. Moreover, some local studies by in-situ transmission electron microscopy[26] showed an electric field driven structural transition from the coexistence of structural symmetries and complex domain configurations to a single orthorhombic symmetry and single-domain state under the applied field. **However, little effort has been made, up to date, to determine the effect that the electric fields produce in compositions situated outside the TP and MPB region.**

Synthesis methods are a determinant factor over the structure and the final properties of lead-free piezo-ferroelectric ceramics. Synthesis and processing variables are not always quite simple and some challenges as stoichiometric control, softer synthesis conditions, adequate grain size, ferroelectric domain size and distribution, sintering conditions and scalability for industrial transfer are still yet to be faced. In most of reported works on BCZT ceramics, the conventional solid-state method is used despite its high thermal conditions and extended processing periods. As an alternative route, the Pechini method has been recently used to obtain enhanced BCTZ ceramic materials[27]. This technique is based on having individual cations complexed with poly-functional organic acids (citric acid is preferred) and ethyleneglycol[28]. The effectiveness of this method comes from maintaining ions mixed at atomic level when they form a polymer resin. Using lower calcination temperatures, very fine powders with narrow crystal size distribution and good stoichiometric control are produced.

In this paper, the effect that the electric field has over the structure and microstructure of $Ba_{0.9}Ca_{0.1}Ti_{0.9}Zr_{0.1}O_3$ (BCTZ) ceramics obtained by Pechini synthesis route was analyzed by means X-ray diffraction and dielectric permittivity curves as a function of the temperature, which provided information on structural and polar evolution at global level. A FE-SEM and confocal Raman spectroscopy and imaging study was also carried out in order to get a more detailed insight at local structural level and spatially resolve this effect. The results are correlated with the ferro-piezoelectric

characteristics of BCTZ ceramics. This research contributes to the understanding of (Ba,Ca)(Ti,Zr)O_3-based ceramics, expanding its applications range.

METHODS AND EXPERIMENTAL DETAILS

BCTZ powders were prepared by Pechini method as reported elsewhere[27]. $Zr(OC_3H_7)_4$ (70% in 1-propanol) and $Ti[OCH(CH_3)_2]_4$ were mixed using absolute ethyl alcohol (99.9%) as solvent. Also, $(CH_3COO)_2Ba$ (99.0%) and $Ca(NO_3)_2 \cdot 4H_2O$ (99.8%) were mixed using deionized water and added to the first solution. Immediately, citric acid ($C_3H_4(COOH)_3$ - 99.5%) and ethylene-glycol ($C_2H_6O_2$ - 99.0%) in a 1:3 molar ratio was incorporated to the global solution. This solution was stirred at room temperature for 30 min. The mixture was heated at 60°C until it gradually became transparent. After that, the temperature was raised to 70°C for evaporating solvents, until a yellow viscous resin was obtained. Then temperature was raised again to 85°C to promote the polymerization of the material. The resin was pre-calcined at 300°C for 30 min obtaining dark-brown powders. The powders were further calcined at 700°C for 1h and ball milled for 8h with zirconia ball media and alcohol. After that, they were dried and pressed into pellets of 13 mm diameter. Pressed samples were sintered at 1275°C for 5h.

The crystal structure of the BCTZ ceramics was examined by X-ray diffraction (XRD) at room temperature using a Bruker D8 Advance diffractometer (Bruker AXS GmbH, Karlsruhe, Germany; Cu $K\alpha_1$ radiation, λ = 1.5406 Å) and a one-dimensional position-sensitive silicon strip detector (Lynx eye, Bruker AXS GmbH, Karlsruhe, Germany). The data were collected from 2θ = 20 to 120° with 40 kV and 40 mA in the X-ray generator, step = 0.02° 2θ and 5s integration time to carry out a Rietveld analysis. The TOPAS software was used for this purpose (Academic Version 4.2). SRM-NIST 660b (LaB_6) was used to model the contributions of the instrument. The Cu-Kα X-ray emission profile was modeled with the one reported by G. Hölzer et al.[29]. The parameters used in refinements included polynomial terms for modeling of the background, the lattice parameters, terms indicating the position and intensity of the "tube tails", specimen displacement, structural symmetry parameters, and the width of a Lorentzian profile for modeling the average crystallite size. Last feature was modeled in reciprocal space with a symmetrized harmonics expansion[30]. The standard deviations are shown by the variation in the last digit, given in parentheses in the text; when they correspond to Rietveld refined parameters, the values are not estimates of the probable error in the analysis, but only of the minimum possible probable errors based on a normal distribution[31].

The size and morphology of grains and ferroelectric domains of the samples was studied by Field Emission Scanning Electron Microscope (JEOL-J7600f, Tokyo, Japan).

Samples were polished and silver electrodes were painted in both circular faces and annealed at 600°C for 30 min for the die-, ferro- and piezo-electric measurements. The ceramics were poled at room temperature under 3kV/mm for 30 min.

The dielectric permittivity (ε_{33}^{T}) and losses (*tan* δ) were measured in-situ on heating at a model HP4194A precision impedance analyzer (Hewlett-Packard, Palo Alto, CA, USA) before and after poling. Disks were heated using a computer-controlled electrical furnace (Thermo Fisher Scientific Inc., Waltham, MA, USA) at a rate of 3°C/min from room temperature up to 200°C.

The piezoelectric constant d_{33} was measured quasi-statically, 24h after the poling process using a d_{33}-meter (APC International, Mackeyville, PA, USA). The d_{ij}, g_{ij} , e_{ij} and h_{ij} piezoelectric coefficients, the electromechanical coupling factors and the frequency numbers, *k and N,* the elastic compliances s_{ij}^{E} and stiffness c_{ij}^{E}, as well as the dielectric permittivity at the resonance frequency were calculated using an automatic iterative method of analysis of the complex impedance measurements at an impedance analyzer (model HP4192A-LF impedance analyzer, Hewlett-Packard, Palo Alto, CA, USA) for the radial and thickness modes of resonance[32] of thin disks and shear resonance of thin plates, thickness poled[33].

Ferroelectric hysteresis loops were measured at room temperature using a ferroelectric test system (RT66, Radiant Technologies Inc., Albuquerque, New Mexico, USA) at 100 Hz. Measurements were carried out in-situ as a function of the temperature in steps of 25°C and after 5 min of temperature stabilization.

In order to analyze the domain structure, the ceramic sample was observed using a Field Emission Scanning Electron Microscope, FE-SEM (Hitachi S-4700, Tokyo, Japan), fitted out with Energy Dispersive Spectroscopy, EDS. With this purpose, the surface of the pellets was carefully polished in two steps to obtain mirror finish surfaces. Finally, the ceramic sample was etched by HCl (5% vol.) acid for times between 30s and 1 min at room temperature to reveal the domain patterns.

Experiments were conducted by Confocal Raman Microscope (CRM) coupled with Atomic Force Microscopy (Witec alpha-300RA) on polished ceramic. Raman spectra were collected using a 532 nm excitation laser and a 100x objective lens (NA = 0.95). The incident laser power was 40 mW. The lateral and vertical resolutions of the confocal microscope were about ~250 nm and ~500 nm, respectively. The spectral resolution of the Raman system was down to 0.02 cm^{-1}. The microscopy sample was mounted on a piezo-driven scan platform having 4 nm lateral and 0.5 mm vertical positional accuracy. The piezoelectric scanning table allows steps of 3 nm (0.3 nm in the vertical direction), giving a very high spatial resolution for the Confocal Raman Microscopy. The microscope base was also fitted with an active vibration isolation system, active 0.7–1000 Hz. Collected spectra were analyzed by using Witec Control Plus Software. Raman image (50 µm of width, 50 µm of length) has 100 x 100 spectra of 0.3s of integration time, demanding ~1h for the acquisition of the whole for planar-section. Collected spectra were analyzed by using Witec Control Plus Software.

For experimentation after electric field application, the samples were poled under identical conditions as those for the electrical measurements. Then, the polarization effect was investigated by measuring Raman map on areas previously studied in the virgin ceramic.

RESULTS AND DISCUSSION

1. X-ray Diffraction.

Figure 1 shows the XRD patterns for a sintered disk (**panel a**) and a poled one (**panel b**), after removal of the electrodes at the analyzed face, which have a single perovskite-type crystal structure phase. The reflections are indexed according to the cubic perovskite cell. The wide 200/002 doublet of the unpoled sample, showed in the magnified angle interval of **Figure 1c**, indicates coexistence of symmetries. It was reported previously[26] that for BCTZ with x=0.15 the rhombohedral, orthorhombic, tetragonal, and cubic coexisting polymorphs are almost indistinguishable in terms of lattice parameters and energetic barriers. Therefore, these ceramics are extremely responsive to the poling fields giving place to high piezoelectric activity. Rietveld analysis of the patterns was made assuming coexistence of quasi-cubic-rhombohedral (*R3m*) and ferroelectric-tetragonal (*P4mm*) symmetries, as suggested in previous literature[19].

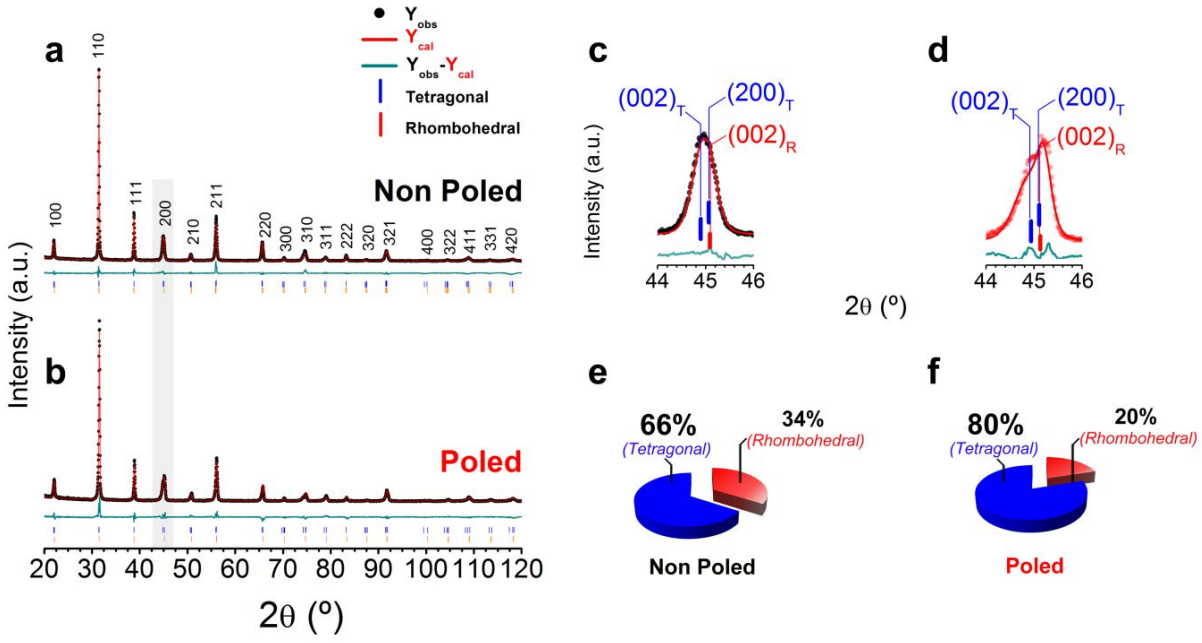

Figure 1. Rietveld refinement for the x-ray diffraction patters of (**a**) unpoled and (**b**) poled BCTZ ceramics. Magnification between 44° and 46° of the XRD patterns for (**c**) non-poled and (**d**) poled BCTZ ceramics. Additionally, the different symmetries distribution before (**e**) and after (**f**) applying an electrical field are indicated at the bottom of each image.

The set of **Figure 1** and **Table 1** displays the Rietveld analysis and results of for both types of samples, before and after poling. Cell parameters and volume, crystal strain for each of the coexisting symmetries is shown, together with the percentage of each one and the quality factor (*Rwp*) of the fit are shown in **Table 1**. For the unpoled sample there is a 66% of ferroelectric *P4mm* symmetry, see **Figures 1c-**

-e. Under the electric field is expected the ferroelectric/ferroelastic domain reorientation. For this symmetry, it is also observed an increase of the c parameter and the c/a ratio (from 1.0037 to 1.0061) induced by the field. All coexisting symmetries experience an increase in the crystal strain in poled samples with respect to unpoled ones. The reduction in the volume of the cell indicates that the structure is under the intergranular stress generated at the poling process due to the ferroelastic character of the tetragonal ferroelectric domains. Besides, data in **Table 1**, as well as **Figures 1d-f**, show that there is an increase of the percentage of the ferroelectric *P4mm* symmetry (to 80%), at the expenses of the quasi-cubic *R3m* one, when the electric field is applied to the sample. Then, it is evidenced at global structural level for this composition, as observed for BCZT with x=0.15 in the literature[19,20,26], that a field induced phase transition takes place, involving a change of crystal symmetry.

Table 1. Refined structural parameters and quality factor, *Rwp*, of the refinement for the unpoled/poled (BCTZ) ceramics using a tetragonal *(P4mm)* + rhombohedral *(R3m)* phase coexistence model.

Space Group / Property vs. Sample type	**Rhombohedral *(R3m)***				**Tetragonal *(P4mm)***					*Rwp*
	Parameter (Å)	Volume (Å³)	Avg. Strain	Fraction (%)	Parameter (Å)		Volume (Å³)	Avg. Strain	Fraction (%)	
	a = b = c				a = b	c				
Non-poled	4.0152(2)	64.7312	0.1881(2)	34	4.0165(2)	4.0317(1)	65.0431	0.4173(6)	66	12.682
Poled	4.0129(2)	64.5841	0.3867(1)	20	4.0135(2)	4.0382(2)	65.0167	0.8594(3)	80	12.147

2. Scanning Electron Microscopy and Energy Dispersive Spectroscopy

Grain Morphology and Compositional Determination at Local Scale

Figure 2 shows the low resolution (LR) SEM results from the fracture surfaces analyzed. As already reported[27], Pechini method allowed synthesizing BCTZ at low temperature and production of dense ceramics with sintering conditions as moderate as 1275°C for 5h.

It must be noted that sintering these ceramics at relatively low temperatures is a challenging task, involving modification of the composition. Nowadays, state of the art on low temperature processing using conventional ceramic technology, including CeO_2 addition, calcined at 1250°C and sintered at 1350°C for 4h[34] or including MnO addition, calcined at 1100°C for 4h and sintered at 1350°C[35].

The microstructure evolution of the ceramic sintered was investigated by characterizing FE-SEM images. The sintered sample is composed by grains with nearly cuboidal morphology (**Figs. 2a-b**). It is possible to observe that these crystals have grown considerably. The pictures reveal an average grain size of ~20 μm. This grain size is much higher than the one commonly obtained at lower sintering

temperatures, allowing us to perform studies on the development of domain structure induced by electric field.

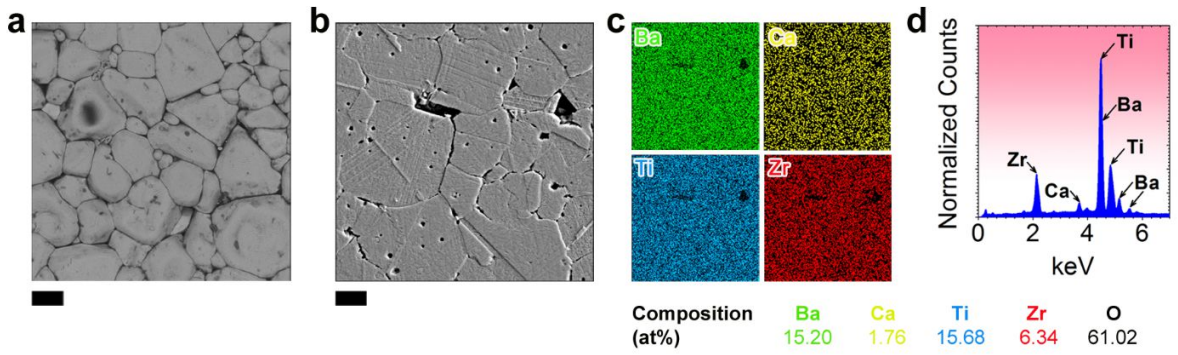

Figure 2. SEM micrograph of the (**a**) fracture surface and (**b**) polished and thermally etched surface of the ceramics sintered at 1275°C-5h. EDX spectrum (**c**) correspond to micrograph (**b**). The table localized at the bottom of (**d**) represents the composition, from EDX spectrum, corresponding to micrograph (**b**), expressed as the atomic percentages of elements. The scale bars in (**a**) and (**b**) corresponds to 10 μm.

To test the compositional homogeneity of the sample with high lateral resolution, the distribution of the different elements involved in the ceramic matrix was characterized using the energy-dispersive X-ray analysis (EDX), as shown in **Figure 2c**. From these figures, we can note that the Ba, Ca, Ti, and Zr elements are homogenously distributed at local scale. Additionally, **Figure 2d** illustrates the EDS spectrum corresponding to the matrix phase and the composition analysis is also summarized in the included table. These data unambiguously confirm that the composition is very close to nominal composition of the BCTZ system.

Identification of the Domain Structure by Field Emission Scanning Electron Microscope.

To analyze the domain structure, several Field Emission Scanning Electron Microscope images were taken over the chemically etched sample. Low-resolution (LR) micrograph (**Figs. 3a-b**) shows the complex structure of domains in the sintered and chemically etched sample. Regarding morphology, three types of domains can be identified in BCTZ ceramic: (*i*) lamellar-like [marked by the red arrow], (*ii*) needle-like [signaled by the green arrow], and (*iii*) watermark shaped [denoted by the yellow arrow]. These are labelled in **Figures 3a-b** as La Ds, Ne Ds, and Wm Ds, respectively. Additionally, in the **panel c** the domain width (*d*) value, which presents a *d* value of ~1 μm, is marked in white color. High-resolution (HR) images (**Figs. 3c-d**) display a lamellar-like domain structure, already reported for $BaTiO_3$ single crystals[36,37] or KNN-based[38,39]. Additionally, needle-like domain structure is observed, the needlepoints terminating at grain boundary. Finally, some other features, like the presence of watermarks could be related to the existence of 180º ferroelectric domain walls[38,40].

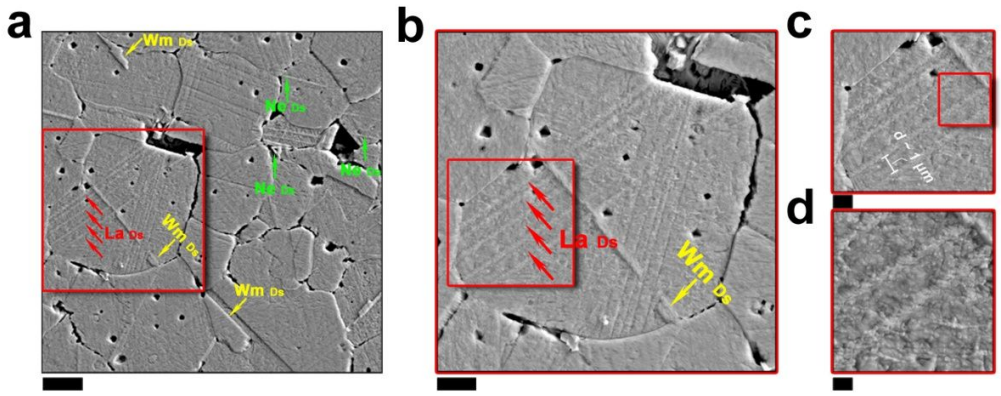

Figure 3. LR-SEM micrographs showing the main morphology of the domain structure of BCTZ ceramic. Magnification increases from panel (**a**) to panel (**d**) so that scale bars in (**a**) correspond to 10 µm, in (**b**) to 5 µm, in (**c**) 1 µm and in (**d**) to 500 nm, which correspond to the regions marked as red rectangles.

Therefore, the domain structure is mainly composed of striped regions, vertically aligned in the image, presumably containing in their interior 180° parallel domains. The most characteristic domain structure (in this particular case, the lamellar-like domains) is mainly constituted of ~1 µm width domains, which appear alternately (see the areas marked on the red box in the **panels (c) and (d)** of the **Figure 3**). Considering a classical approach for ceramic samples, it is well known that the domain width, d, is related to the grain size, G, as $d \sim \sqrt{G}$[41]. Considering here a~20 µm, the d value should be ca. 4.5 µm. However, as we have seen above, the principal domain structure is constituted by domain with d values (~1 µm) due to its boundary conditions, which would be governed by the intergranular stress. It is worth highlighting here that the presence of the stress is resolved by increasing the domain walls density, resulting in a drastic diminution of the domain width as seen in **Figure 3d**.

3. Confocal Raman Microscopy

To determine the electrical field effect on the ceramic microstructure, experiments were performed by confocal Raman microscopy (CRM). As above mentioned, the BCTZ system has 66% content of tetragonal symmetry (**Table 1**) with a space group *P4mm* at room temperature. **Figure 4a-b** depicts spatial Raman maps of the ceramic sample before and after applying an electrical field, respectively. Features such as Raman peak intensity, peak width or Raman shifts are fitted with algorithms in order to compare information and to represent the derived Raman images. The Raman modes of $BaTiO_3$-based materials are assigned and summarized in the ***Supplementary Table S1***, in which are displayed both symmetry and nature (first and second order). The fitted spectrum of BCTZ shows six vibration modes centered at 162, 230, 305, 515, 545 and 723 cm^{-1}, which are in agreement with reported data by other researches[42-44] for a perovskite structure with tetragonal symmetry. In both cases, this phase

is represented in red color in **Figures 4a-b.** In the **Figures 4c-d**, the numbers next to the vibrational peaks represent each of the above Raman modes (see ***Supplementary Table S1***). The first mode at about 162 cm^{-1} is attributed to the Ca–O or/and Ba-O bonds of the A-site vibration in the perovskite of general formula ABO_3. The second and third band situated in the range between 210 and 305 cm^{-1} are associated with the vibration of the BO_6 group and are observed in many perovskite materials[42,43], while the modes observed in the range between 440 and 620 cm^{-1} are controlled by vibrations involving mainly oxygen displacements in the B-O bonds of the BO_6 octahedra. The last Raman is contributed to A–O bonds. Note that clear differences can be observed in the Raman shift of both spectra (that is, for the ceramic before and after polarization process), particularly in the 440 to 620 cm^{-1} region (see details for bands **4** and **5** in **Fig. 4c-d**).

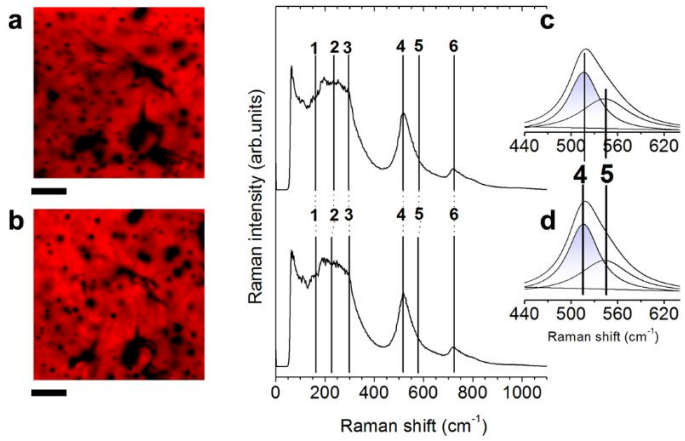

Figure. 4. Confocal Raman Microscopy surface images resulted from mapping the different single Raman spectra obtained from each pixel of ceramic sample before (**a**) and after (**b**) applying an electrical field. Raman spectra having same spectral shift for the Raman modes are identified using the same color. The intensity of the color is correlated with the Raman intensity. Scale bar is 10 µm. Average Raman spectrum of ceramic sample corresponding to the before (**c**) and after (**d**) poling state. In both cases, the Raman spectrum is fitted as the sum of six Lorentzian modes, which are signaled in the panel **a** as **1**, **2**, **3**, **4**, **5** and **6**. The inserts show magnified Raman spectra, which fitted by the sum of two Lorentzian peaks, ascribed to the **4** and **5** Raman modes, respectively.

It is well stablished that different crystallographic orientations of the spontaneous polarization result into noticeable variations of the Raman shift because of the distortion of the oxygen octahedra originated on the ceramic by application of an electric field. For illustrative purposes, in **Figures 5a** and **f**, we show the spatial maps of the Raman shift signal of the **4** mode for the ceramic before (**Fig. 5a**) and after (**Fig. 5b**) the application of the field. To get further insights into this feature, it is displayed a statistical analysis of the pixel number versus mode Raman shift associated with the vibration of the BO_6 group (assigned as **4** in **Fig. 4c-d**). Note that an evident decreasing in the Raman shift of this mode occurs

after application of the electric field. This behavior implies that the field alters the observed vibration frequencies, shifting the Raman mode (assigned as **4** in **Figs. 4c-d**) to lower wavenumber due to a decrease in the strength of the constant force, caused by the lengthening of the distance between B^{5+} type ions and their coordinated oxygens[39,45,46]. It fact, this is evidenced by the color change in the spatial maps of the Raman shift signal (**Figs. 5c-d**) caused by the poling process. More specifically, we can infer that the lengthening of the B-O bond distance induced by the application of the electric field provokes a net increase on the structural strain of the BCTZ ceramic. This result is in good agreement with the obtained from XRD (**Table 1**).

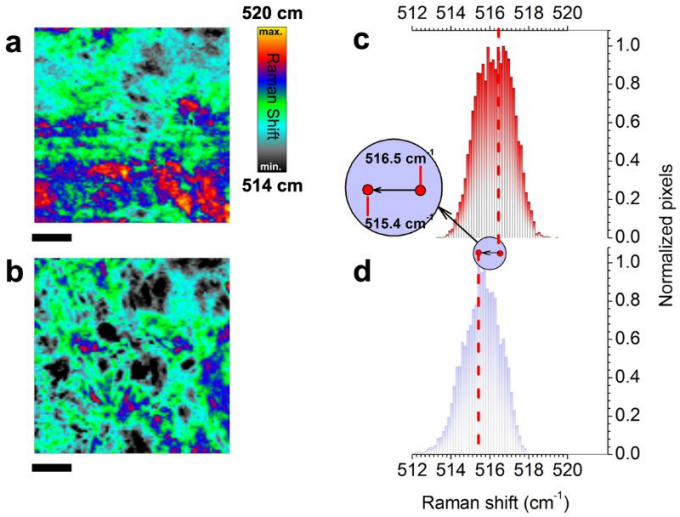

Figure 5. Spatial map of the Raman shift signal showing the Raman shift at each pixel corresponding to the Raman mode **4** on the ceramic sample before (**a**) and after (**b**) applying an electrical field. The color code of the bar corresponds to maximum (520 cm^{-1}) and minimum (514 cm^{-1}) values of Raman shift of the **Figs. c-d**. Scale bar, 10 µm. Statistical analysis of the pixel number versus mode Raman shift associated with the vibration of the BO_6 group and centered in frequency range between ~520 and ~514 cm^{-1} before (**c**) and after (**d**) applying an electrical field.

4. Dielectric permittivity vs. temperature

Phase transitions that involve a change of the polar state (from non-polar or weakly polar to polar or between polar phases) of the crystals are accompanied by a subsequent change of dielectric permittivity. The measurement of dielectric permittivity curves (at different frequencies) above the ferroelectric transition to the paraelectric state provides information about the local polar structure and about phase transitions.

Dielectric permittivity (ε_r) and losses ($tan\ \delta$) as a function of the temperature on heating of the non-poled and poled ceramics are shown in **Figure 6a**. The first effect caused by poling the sample (circle marked with **1** in **Fig. 6a**) is the permittivity decrease, related with the domain orientation and higher

amount of the polar ferroelectric *P4mm* symmetry content (**Table 1**). The measurement of the poled sample on heating shows a slight change of slope of the permittivity (circle marked with **2** in **Fig. 6a**) that would correspond to a phase transition between polar phases before the transition to the paraelectric one.

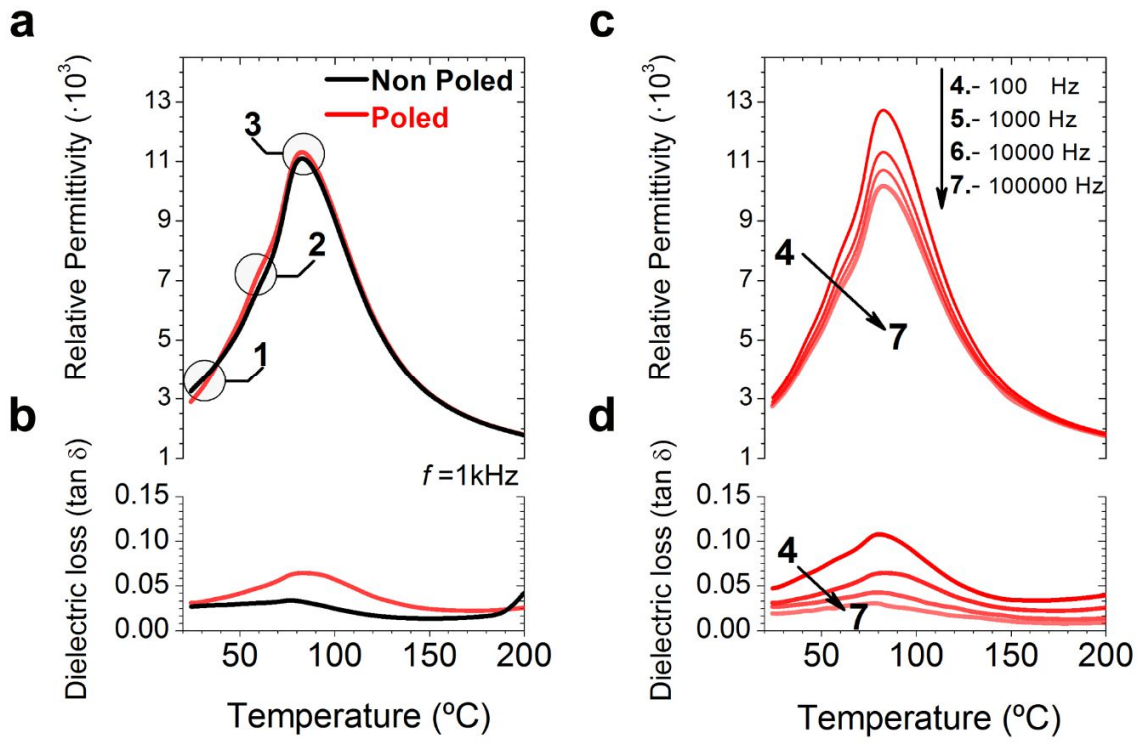

Figure 6. Dielectric permittivity (**a**) and losses (**b**) measured for BCTZ poled/non-poled ceramics (1 kHz). Dielectric permittivity (**c**) and losses (**d**) as a function of frequency of the poled BCTZ ceramics.

This transition is usually ascribed for BCZT ceramics to FE-rhombohedral to FE-tetragonal (R-T) ferroelectric phases evolution[47]. This feature of the permittivity curve of the poled ceramic could be an insight of that the quasi-cubic rhombohedral *R3m* content in the unpoled ceramic, not only diminishes under the action of the applied electric field, but also, at least partly, transforms into FE-rhombohedral *R3c*. Our X-ray experiments do not have the required resolution as to clarify this point. This symmetry upon heating has a transition to FE-tetragonal, however the quasi-cubic *R3m* would not experience this transition and, consequently, the permittivity curve of the unpoled ceramic do not show this feature. The third effect (circle marked with **3** in **Fig. 6a**), a slight increase of the permittivity at the temperature of the maximum is related with the differences in ionic conductivity, mainly related with oxygen vacancies and their ordering in the structure between both states. Such effect causes in the poled ceramic the frequency dispersion observed in **Figures 6c-d**. The dispersion is usually ascribed to a dielectric relaxor behavior. Relaxors have diffuse phase transitions (as the one showed in **Figs. 6c-d**), that are generally characterized

by (**a**) broadening in the dielectric permittivity versus temperature curve; (**b**) a relative large separation (in temperature) between the maximum of the real dielectric constant and imaginary dielectric loss parts; (**c**) a deviation from the Curie-Weiss law near the maximum dielectric permittivity (T_m); and (**d**) frequency dispersion of both ε_r and *tan* δ in the transition region[48].

5. Ferroelectric Hysteresis Loops

The high density of the BCTZ ceramics studied allows us to measure the ferroelectric response, and, therefore, to attempt a correlation of ferroelectric properties with the observed structural evolution. For a better understanding of the relationships between physical-chemical phenomena involved in building-up a macroscopic polarization and the electromechanical properties of this material, the electric field dependence of polarization (P-E loops) as a function of the applied voltage were measured at room temperature. **Figure 7a** shows the P-E hysteresis loops of BCTZ ceramics recorded at room temperature as a function of increasing applied electric field. Sub-coercive loops show a small ferroelectric contribution with a remnant polarization P_r<2μC/cm^2. As the maximum applied voltage increases, the maximum polarization also increases continuously, but at a lower rate as the loops become well saturated and without conductivity contributions. However, the remnant polarization (P_r) increases up to 10 μC/cm^2 and remains almost unchanged from this point. **The two regimes of polarization increase are usually ascribed to the 180º domains reorientation (easier and taking place at lower fields) and non-180º domains ferroelectric-ferroelastic domains reorientations. Further work on X-ray diffraction as a function of the electric field will be necessary to clarify the importance of the field induced structural transition on these two regimes of polarization building.**

Coercive field values lower than 2 kV/cm indicate the easy polarization mechanism of the material. The low coercive field (E_C) indicates that the ceramic is "soft". The polarization mechanism has two components. One the one hand the ferroelectric-ferroelastic domain walls movements and, on the other, the structural phase transition with change of crystal symmetry, revealed by XRD (**Fig. 1**) and ε_r measurements as a function of the temperature (**Fig. 6**), that promotes ferroelectric phases at the expenses of a, weakly polar, quasi-cubic *R3m*. To evaluate the effect of voltage applied accurately on the ferroelectric properties, the evolution of maximum polarization (P_{max}), P_r and E_C are plotted in **Figure 7b**.

In **Figure 7c**, the hysteresis loops are recorded as a function of the temperature. Values of coercive fields E_C diminish as the temperature increased. As expected, the remnant polarization also decreases, but with a higher rate (**Fig. 7d**) that the maximum polarization of the loop. This indicates that there is an increasing contribution of polarization that it is only achievable under the application of the electric field[49], non-ferroelectric polarization arising from non-correlated polar nanoregions. There is, consequently and increasing slim loop character of the cycles. Moreover, it is noticeable that there are well defined hysteresis loops at higher temperatures than the one corresponding to the maximum

dielectric permittivity. This is also related with the stronger frequency dispersion of the permittivity curves (**Fig. 6c**) from the anomaly at ~60ºC (marked as **2** in **Fig. 6a**) revealing the increasing relaxor character of the material from that temperature and the diffuse character of the thermally induced transition from the ferroelectric phase[50].

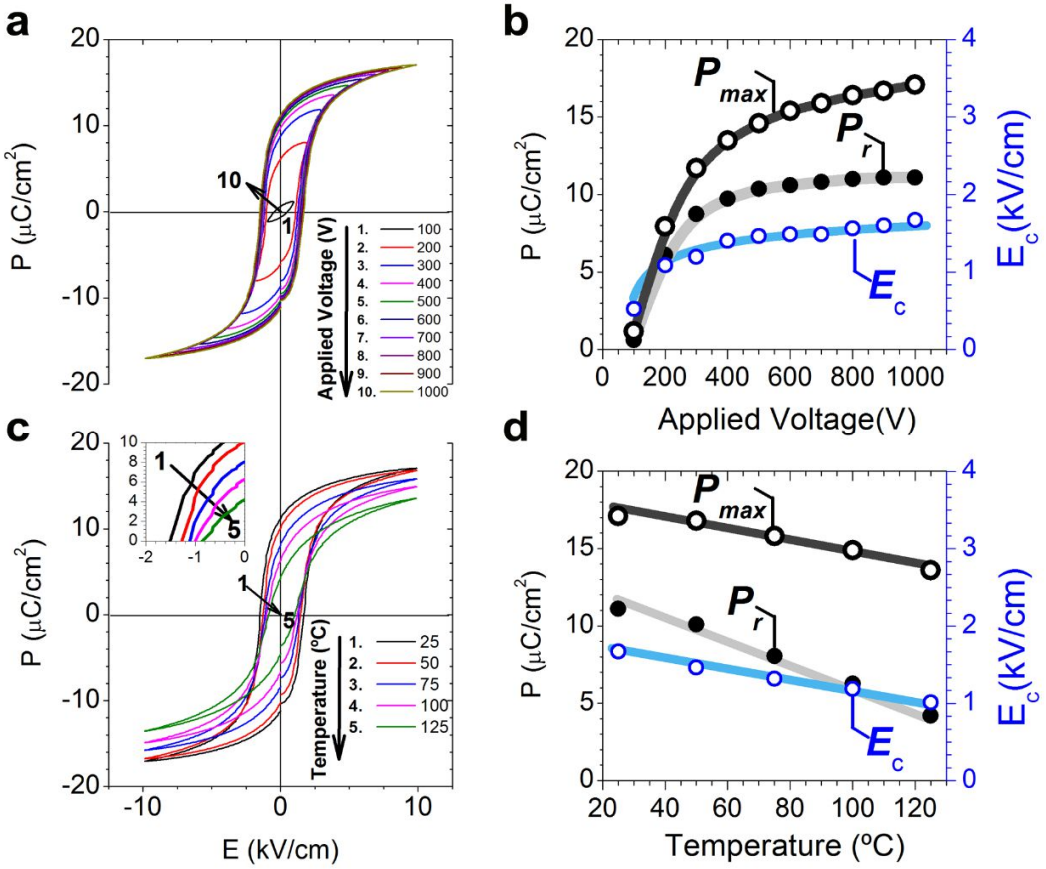

Figure 7. Ferroelectric hysteresis loops of BCTZ ceramic as function of the (**a**) applied voltage and (**b**) remnant polarization (P_r), saturated polarization (P_{max}) and coercive field (E_C) values as function of the **(a)** applied voltage. Saturated loops of BCTZ ceramic (**c**) and (**d**) evolution of P_r, P_{max} and E_C as a function of the temperature.

6. Electromechanical resonances

Figure 8 show an alternative representation of the complex impedance at resonance for the fundamental radial (**Figs. 8a**) and thickness (**Figs. 8b**) extensional modes, of a thin disk, thickness poled (t=1 mm and D=9.74 mm) at room temperature. The representation usually found in the literature is the curves of the modulus and phase angle of the complex impedance (Z*). **Figure 8** shows the peaks of the real part (Resistance (R)) of the complex impedance (Z*) and the real part (Conductance (G)) of the complex admittance (Y*), the inverse of the impedance. These peaks are used for the determination of the

410 frequencies of interest for the iterative analysis of the complex impedance curve at the electromechanical
411 resonance in the determination of the piezoelectric, dielectric and elastic material coefficients. Also,
412 **Figure 8c** shows the shear mode of a thin plate, thickness poled, that initially had 1 mm thickness (t), and
413 lateral dimensions 8.1 and 5.9 mm. Shear modes of plates used for material characterization often show a
414 high degree of modes coupling. This plate was thinned down to 0.5 mm, following the coupling of the
415 shear and lateral resonances. **Figure 8c** show the R and G peaks for the shear mode of the thin plate of
416 0.75 mm thickness, chosen for the calculation of the material parameters because it shows a virtually
417 monomodal resonance. This is a necessary condition for the validity of the calculation of the materials
418 coefficients shown in **Table 2** using the iterative analysis of the complex impedance at resonance[33]. **Figure**
419 **8** also shows (dotted lines) the reconstructed spectra carried out by insertion of the calculated material
420 parameters in the expression of the complex impedance for each given resonance[32,35]. The accuracy of this
421 reconstruction is considered as a quality test for the validity of the material parameters, which is high for
422 the three resonances considered. The piezoelectric activity in each mode is related with the peak
423 separation.

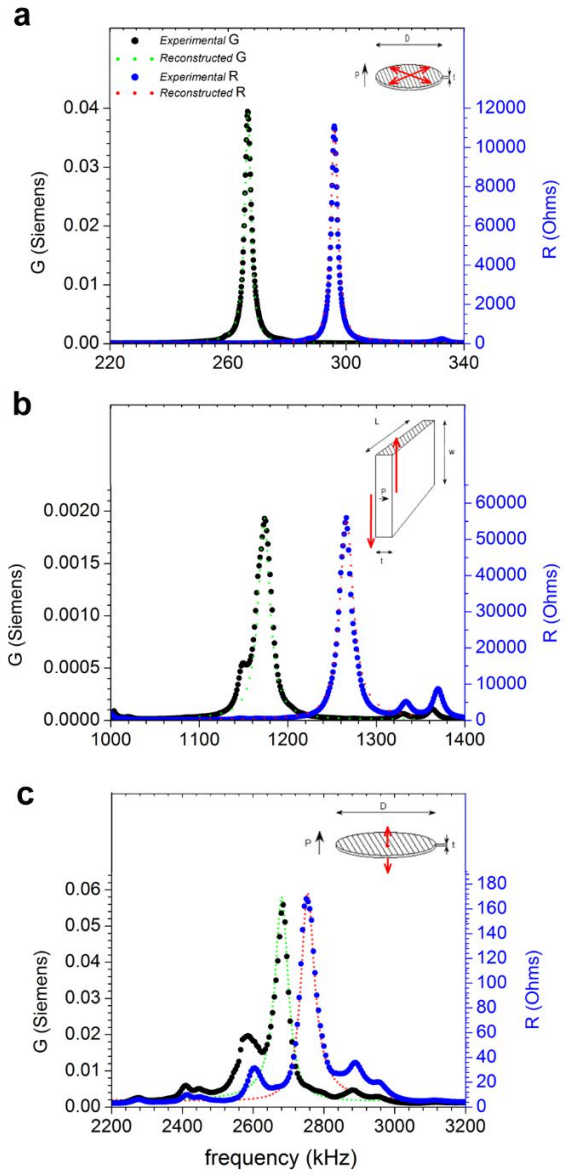

Figure 8. Peaks of the Resistance (R) and the Conductance (G) at room temperature for the fundamental radial (**Figs. 8a**) and thickness (**Figs. 8c**) extensional modes of a thin disk (t= 1 mm and D=9.74 mm) thickness poled. R and G shear mode **(Fig. 8b)** of a, thickness poled, thin plate of 0.75 mm thickness (t), and lateral dimensions 8.1 and 5.9 mm.

Table 2. Piezoelectric, dielectric and elastic complex coefficients at resonance of BCZT ceramics (ρ=5.70 g/cm³). Electromechanical coupling factors and frequency numbers are also shown.

Elastic stiffness constants ($c_{ij}^* = (c_{ij})_{real} + i(c_{ij})_{img}$) ($10^{10}$ N/m²)

	c_{11}^D	c_{33}^D	c_{55}^D	c_{11}^E	c_{33}^E	c_{55}^E
real	12.23	16.26	4.46	10.54	16.26	4.22
imaginary	0.116	0.275	0.065	0.098	0.276	0.059

Elastic compliance constants ($s_{ij}^* = (s_{ij})_{real} + i(s_{ij})_{img}$) ($10^{-12}$ m^2/N)

	s_{11}^D	s_{12}^D	s_{55}^D	s_{11}^E	s_{12}^E	s_{55}^E	s_{66}^E
real	8.54	-1.77	21.45	11.12	-2.94	20.75	20.61
imaginary	-0.080	0.015	- 0.351	-0.088	0.006	-0.254	-0.191

Piezoelectric Coefficients

	$d_{ij}^* = (d_{ij})_{real} + i(d_{ij})_{img}$ (10^{-12} N/C)			$e^* = (e)_{real} + i(e)_{img}$ (C/m²)	$g_{ij}^* = (g_{ij})_{real} + i(g_{ij})_{img}$ (10^{-3} Vm/N)			$h_{ij}^* = (h_{ij})_{real} + i(h_{ij})_{img}$ (10^8 V/m)	
	d_{33}	d_{31}	d_{15}	e_{33}	g_{33}	g_{31}	g_{15}	h_{33}	h_{15}
real	390[d]	-143	278	12.25	3.90[d]	-7.20	12.64	8.81	6.13
imaginary	----	3.28	-21	0.475	---	-0.142	0.056	0.464	0.064

([d]) Not calculated from resonance curves

Electromechanical Coupling Factors (k) and frequency numbers (N (kHz.mm))

k_{31}	N_{31}	k_{15}	N_{15}	k_t	N_T	k_p	N_p
0.32	---	0.31	1491	0.24	2689	0.50	2597

Dielectric Permittivity

	ε_{33}^T	ε_{33}^S	ε_{11}^T	ε_{11}^S
real	3397	2876	3375	2864
imaginary	-27	-22	-24	-18

Table 2 displays the calculated piezoelectric, dielectric and elastic complex coefficients at resonance of the studied BCZT ceramics. Electromechanical coupling factors and frequency numbers are also shown. Overall this is one of the most complete set of parameters known for this material that includes the three types of losses, dielectric, piezoelectric and elastic. Noticeably the planar coupling factor (k_p=50%) and the piezoelectric d_{33} coefficient (390 pC/N), obtained from the planar mode, are high enough as to consider this lead-free ceramic a suitable candidate for replacement of PZTs.

CONCLUSIONS

In conclusion, the effects that the polarization process has on the structure, microstructure and electrical properties of prepared BCTZ ceramics were investigated. The applied electric field induces changes in rhombohedral-tetragonal relative content, as revealed by X-ray diffraction and permittivity measurements as a function of the temperature. For the first time, the field-induced phase transition phenomenon is reported outside of the Triple Point and Morphotropic Phase Boundary.

A confocal Raman spectroscopy and imaging study carried out on both types of samples reveals that, upon application of an electric field, the $E(LO_3) + A_1(LO_2) + E(TO_4)$ mode of the Raman spectra shifts

to lower frequencies, indicating a reduction of the bonding force between the ions at the B-site of the perovskite (Ti^{4+}, Zr^{4+}) and the oxygen ions of the octahedron for the poled samples. Besides, the spatially resolved mentioned mode of the Raman spectra shows a narrower distribution in the poled sample, monitoring the effect of alignment of the polarization in the direction of the field. These characteristics are related with the complex ferroelectric domain distribution.

Moreover, a net increase on the structural strain and intergranular stress are generated. This last characteristic increases the domain walls density at expenses of domain width, promoting a domain orientation that enhances the piezo-ferroelectrical ceramic response.

ACKNOWLEDGEMENTS

A Reyes-Montero gratefully thanks CONACyT-México for providing a PhD scholarship, as well as F González and LDRX (T-128) UAM-I for XRD measurements. M E Villafuerte-Castrejón kindly acknowledges PAPIIT-UNAM (IN102715) for financial support. This research was partially carried out during the sabbatical year, at ICMM-CSIC (Madrid, Spain), of M E Villafuerte-Castrejón (PASPA-UNAM and CONACyT-México) and a short stay of A Reyes-Montero (CONACyT-México). Part of this work was supported by the Spanish National Research Council (CSIC) under project NANOMIND CSIC 201560E068. F Rubio-Marcos is also indebted to MINECO for a 'Ramon y Cajal' contract (ref: RyC-2015-18626), which is co-financed by the European Social Fund.

COMPETING FINANCIAL INTERESTS

The authors declare no competing financial interests.

REFERENCES

1. J. Rodel, W. Jo, K. Seifert, E. Anton, T. Granzow, and D. Damjanovic, *J. Am. Ceram. Soc.*, 2009**, 92**, 1153.
2. Z. L. Wang, *J. Phys. Chem. Lett.*, 2010**, 1**, 1388-1393.
3. E. Li, H. Kakemoto, T. Hoshina and T. Tsurumi, *Jpn. J. Appl. Phys.*, 2008, **47**(9), 7702-77-06.
4. A. Mathieson and D. A. DeAngelis, *IEEE Trans. UFFC*, 2016, **63**(1), 156 - 164.
5. J. Wu, D. Xiao and J. Zhu, *Chem. Rev.*, 2015, **115**(7), 2559–2595.
6. J. Wu, Z. Fan, D. Xiao, J. Zhu and J. Wang, *Prog. Mater Sci.*, 2016, 84, 335-402.
7. E. Taghaddos, M. Hejazi and A. Safari, *J. Adv. Dielect.*, 2015, **5**(2), 1530002.
8. K. Ylli, D. Hoffmann, A. Willmann, P. Becker, B. Folkmer and Y. Manoli, *Smart Mater. Struct.*, 2015, **24**, 025029.
9. J. Granstrom, J. Feenstra, H. A. Sodano and K. Farinholt, Smart Mater. Struct., 2007, **16**, 1810-1820.
10. K. Kalyanaraman and J. Babu, *Proceedings of the World Congress on Engineering and computer Science*, 2010, **2.**

11. H. B Fang, J. Q. Liu, Z. Y. Xu, L. Dong, L. Wang, D. Chen, B. C. Cai and Y. Liu, *Microelectronics Journal*, 2006, **37**(11), 1280-1284.
12. M. Algueró, C. Alemany, L. Pardo and A. M. González. *J. Am. Ceram. Soc*., 2004, **87**(2), 209-215.
13. J. Wu, D. Xiao, W. Wu, Q. Chen, J. Zhu, Z. Yang and J. Wang, *Scripta Materialia*, 2011, **65**(9), 771-774.
14. W. Liu and X. Ren, *Phys. Rev. Lett.*, 2009**, 103**, 257602.
15. Y. K. Choi, T. Hoshina, H. Takeda and T. J. Tusumi, *J. Ceram. Soc. Jpn*. 2010, **118**(10) 881-886.
16. D. Damjanovic, *Appl. Phys. Lett.*, 2010**, 97**, 062906.
17. A. K. Kalyani, K. V. Lalitha, A. R. James, A. N. Fitch and R. Ranjan, *J. Phys. Condens. Matter*. 2015**, 27**, 072201.
18. J. Gao, X. Hu, L. Zhang, L. Fei, L. Zhang, Y. Wang, Y. Hao, L. Zhong and X. Ren, *Appl. Phys. Lett.*, 2014**, 104**, 252909.
19. K. Brajesh, K. Tanwar, M. Abebe and R. Ranjan, *Phys. Rev. B*, 2009**, 92**, 257602.
20. J. Wu, D. Xiao, W. Wu, Q. Chen, J. Zhu, Z. Yang and J. Wang, *J. Eur. Ceram. Soc.*, 2012**, 32**, 891-898.
21. M. Hinterstein, J. Rouquette, J. Haines, P. Papet, M. Knapp, J. Glaum and H. Fuess, *Phys. Rev. Lett.*, 2011**, 107**, 077602.
22. C. Chen, X. Zhao, Y. Wang, H. Zhang, H. Deng, X. Li, X. Jiang, X. Jiang and H. Luo, *Appl. Phys. Lett.*, 2016, **108**, 022903.
23. J. Shi, W. Tian, X. Liu and H. Fan, *J. Am. Ceram. Soc.*, 2017, **100**, 1080–1090.
24. R. Vivar-Ocampo, L. Pardo, D. Ávila, E. Morán, A. M. González, L. Bucio and M. E. Villafuerte-Castrejón, *Materials* 2017, **10**(7), 736.
25. L. Zhang, M. Zhang, L. Wang, C. Zhou, Z. Zhang, Y. Yao, L. Zhang, D. Xue, X. Lou and X. Ren, *Appl. Phys. Lett.*, 2014**, 105**, 162908.
26. H. Guo, B. K. Voas, S. Zhang, C. Zhou, X. Ren, S. P. Beckman, and X. Tan, *Phys. Rev. B*, 2014**, 90**, 014103.
27. A. Reyes-Montero, L. Pardo, R. López-Juárez, A. M. González, M. P. Cruz and M. E. Villafuerte-Castrejón, *J. Alloy. Comp.*, 2014**, 584**, 28-33.
28. M. Pechini, U.S. Patent. 33300697, July 1967.
29. G. Hölzer, M. Fritsch, M. Deutsch, J. Härtwig and E. Förster, *Phys. Rev. A*, 1997**, 56**, 4554.
30. M. Järvinen, *J. Appl. Cryst.*, 1993**, 26**, 525-531.
31. E. Prince, *J. Appl. Cryst.*, 1981**, 14**, 157-159.
32. C. Alemany, A. M. González, L. Pardo, B. Jiménez, F. Carmona and J. Mendiola, *J. Phys. D: Appl. Phys.*, 1995**, 28**, 945-956.
33. L. Pardo, A. García, F. Montero and K. Brebøl, *IEEE Trans. UFFC*, 2011**, 58**(3), 646-657.
34. Y. Cui, X. Liu, M. Jiang, X. Zhao, X. Shan, W. Li, C. Yuan, and C. Zhou, *Ceram. Int.*, 2012**, 38**, 4761-4764.
35. M. Jiang, Q. Lin, D. M. Lin, Q. J. Zheng, X. M. Fan, X. C. Wu, H. L. Sun, Y. Wan and L. Wu, *J. Mater. Sci.*, 2013**, 48**, 1035-1041.
36. W. J. Merz, *Phys. Rev*. 1954**, 95**, 690-698.
37. F. Rubio-Marcos, A. Del Campo, P. Marchet and J. F. Fernández, *Nat. Commun.*, 2015**, 6**, 6594.
38. R. López-Juárez, O. Novelo-Peralta, F. González-García, F. Rubio-Marcos and M. E. Villafuerte-Castrejón, *J. Eur. Ceram. Soc.*, 2011**, 31**, 1861-1864.

39. F. Rubio-Marcos, A. Del Campo, R. López-Juárez, J. J. Romero and J. F. Fernández, *J. Mater. Chem.,* 2012, **22**, 9714-9720.

40. Z. Kighelman, D. Damjanovic, M. Cantoni, and N. Setter, *J. Appl. Phys.,* 2002**, 91**, 1495-1501.

41. G. Arlt, *J. Mater. Sci.* 1990**, 25**, 2655-2666.

42. Z. M. Wang, K. Zhao, X. L. Guo, W. Sun, H. L. Jiang, X. Q. Han, X. T. Tao, Z. X. Cheng, H. Y. Zhao, H. Kimura, G. L. Yuan, J. Yin and Z. G. Liu, *J. Mat. Chem. C,* 2013**, 1**, 522-530.

43. P. S. Dobal and R. S. Katiyar, *J. Raman Spectrosc.* 2001**, 33**, 405-423.

44. J. Wu, D. Xiao, W. Wu, Q. Chen, J. Zhu, Z. Yang and J. Wang, *Src. Mater.,* 2011**, 65**, 771-774.

45. F. Bortolani, A. Campo, J. F. Fernández, F. Clemens and F. Rubio-Marcos, *Chem. Mater.,* 2014**, 26**(12), 3838-3848.

46. F. Rubio-Marcos, J. J. Romero, D. A. Ochoa, J. E. García, R. Perez and J. F. Fernández, *J. Am. Ceram. Soc.,* 2010**, 93**, 318-321.

47. D. Xue, Y. Zhou, H. Bao, C. Zhou, J. Gao and X. Ren, *J. Appl. Phys.,* 2011**, 109**, 054110.

48. X. G. Tang, K. H. Chew and H. L. W Chan, *Acta Mater.,* 2004**, 52**, 5177-5183.

49. K. Brajesh, K. Tanwar, M. Abebe and R. Ranjan, *Phys. Rev. B, 2015***, 92**, 224112.

50. L. Jin and S. J. Zhang, *J. Am. Ceram. Soc.,* 2014**, 97**(1), 1-27.